Bio-Design and Manufacturing (2026) 9:318–334
https://doi.org/10.1631/bdm.2500389

RESEARCH ARTICLE

Self-assembled polyoxometalate–phenolic nanodrugs integrated with dissolving microneedles for hypertrophic scar combination therapy

Manyi Du[1] · Ruofei Xu[1] · Xianbin Sun[1] · Haixin Long[1] · Jing Yu[1] · Yilin Zheng[1] · Haijun Chen[1] · Yansheng Lin[2] · Yu Gao[1]

Received: 31 July 2025 / Accepted: 30 November 2025

Abstract

The clinical management of hypertrophic scars (HSs) remains challenging due to their complex etiology and heterogeneous morphology, underscoring the need for multitarget treatment strategies. In this study, we developed a nanocomposite system constructed through the metal–phenolic network–mediated self-assembly of molybdenum polyoxometalate ({Mo_{154}}) and epigallocatechin gallate (EGCG), followed by chitosan encapsulation, to generate chitosan-encapsulated {Mo_{154}}/EGCG (CME) nanoparticles. These nanoparticles were integrated into dissolvable microneedles (CME@MN) to enable transdermal administration. Under near-infrared laser irradiation, CME exhibited a three-pronged therapeutic effect: suppression of collagen overproduction and excessive extracellular matrix (ECM) deposition in human keloid fibroblasts, regulation of proliferation and migration in human umbilical vein endothelial cells, and reprogramming of macrophages toward a proinflammatory M1 phenotype. In vivo, CME@MN patches preferentially accumulated within scar tissue, where they normalized ECM organization, improved collagen fiber rearrangement, and attenuated fibroblast activity through photothermal-enhanced mechanisms while maintaining an excellent safety profile. The CME@MN system represents a potentially transformative approach to HS management by offering a unified platform that simultaneously targets the fibrotic, angiogenic, and inflammatory components of scar pathogenesis.

Manyi Du and Ruofei Xu have contributed equally to this work.

✉ Yu Gao
hellogaoyu@126.com
ygao@fzu.edu.cn

[1] Fujian Provincial Key Laboratory of Cancer Metastasis Chemoprevention and Chemotherapy, College of Chemistry, Fuzhou University, Fuzhou 350116, China

[2] Sanming Integrated Medicine Hospital, Sanming 365001, China

Graphical abstract

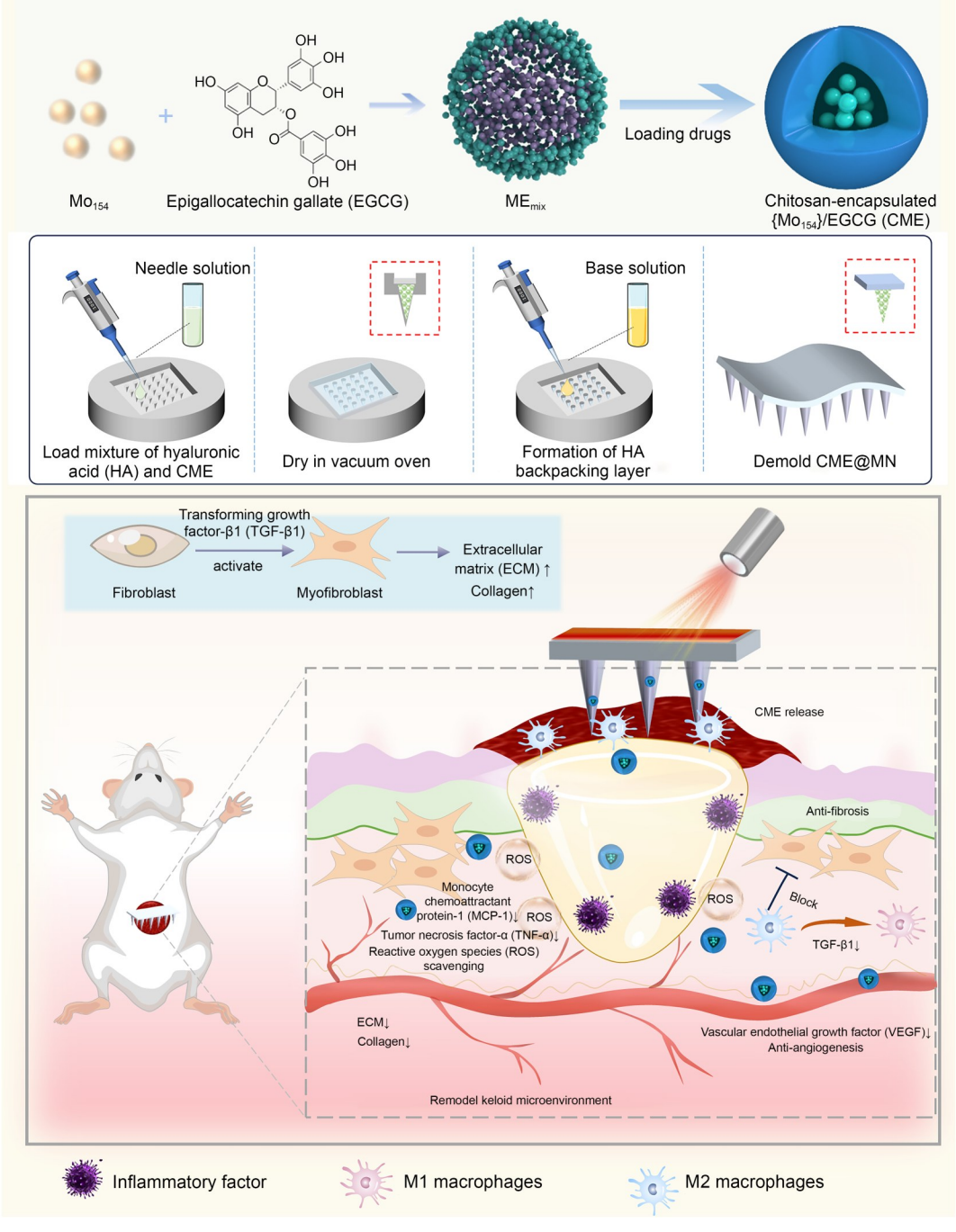

Keywords Hypertrophic scar therapy · Anti-fibrosis · Microneedle · Metal–phenolic network · Polyoxometalate

1 Introduction

Scars are pathological tissues that form during skin repair, involving complex processes such as cell migration, inflammation, innervation, and angiogenesis [1]. Their diverse etiologies and morphologies present significant therapeutic challenges. Hypertrophic scars (HSs), the most common type of pathological scarring, are characterized by excessive proliferation of fibrous connective tissue and abnormal collagen deposition [2]. Beyond cosmetic concerns, HSs often

cause itching, pain, ulceration, and in severe cases, may contribute to secondary malignancies, imposing significant physical and psychological burdens [3].

HS pathogenesis is initiated by immune-mediated inflammation, in which macrophages promote vascular dilation, cell infiltration, and the release of growth factors [4]. Persistent inflammatory responses generate excessive reactive oxygen species (ROS), exacerbating oxidative stress and damaging surrounding cells, including fibroblasts [5]. Under normal conditions, fibroblasts differentiate into α-smooth muscle actin (α-SMA)-expressing myofibroblasts responsible for collagen production [6]; however, sustained α-SMA activation in HS leads to aberrant collagen deposition and fibrosis. This process is further aggravated by vascular endothelial cell-derived factors, including transforming growth factor-β1 (TGF-β1) and vascular endothelial growth factor (VEGF), which stimulate fibroblast proliferation and collagen synthesis [7]. Dysregulated angiogenesis in HS contributes to localized hypoxia and an imbalance in extracellular matrix (ECM) metabolism [8]. Additionally, substantial infiltration of M2 macrophages releases profibrotic mediators, such as TGF-β1 and monocyte chemoattractant protein-1 (MCP-1), further promoting fibrotic tissue deposition [9]. Therefore, effective HS management requires a comprehensive therapeutic approach that simultaneously addresses the fibrotic, angiogenic, and inflammatory components of scar pathogenesis. To date, no integrated treatment platform has been reported to achieve this comprehensively.

Scar management currently employs multiple strategies, including pharmacological interventions, physical therapies, surgical excision, and bioengineering approaches [10]. However, these conventional treatments show limited efficacy and often require repeated applications, imposing significant burdens on patients. Therefore, novel therapeutic platforms are urgently required. Polyoxometalates (POMs) are nanoscale anionic metal-oxide clusters that comprise transition metals such as vanadium, niobium, tantalum, molybdenum (Mo), and tungsten. They have attracted considerable interest due to their notable redox activity and ROS-scavenging capability [11]. Among these, Mo-based POMs are particularly promising due to their exceptional aqueous solubility and near-infrared (NIR) absorption, which enable effective photothermal therapy (PTT) for scar modulation [12]. PTT has been shown to reduce scar thickness and collagen density by remodeling collagen fibers, while NIR light facilitates deeper tissue penetration [13]. Additionally, metal–phenolic networks (MPNs), formed by coordination of natural polyphenols with metal ions, offer significant potential for wound repair [14]. Epigallocatechin gallate (EGCG), a polyphenol with anti-inflammatory, antioxidant, and anti-fibrotic properties [9], can coordinate with metal ions to form functional MPNs [15]. Clinical studies have shown that EGCG can reduce keloid size, suppress proliferative factors, and downregulate fibrotic proteins, highlighting its potential for HS treatment [16]. However, its clinical application is limited by poor tissue adhesion and rapid degradation.

Transdermal delivery offers a promising strategy for HS treatment. Chitosan (Cs), a natural cationic polymer with anti-inflammatory, antibacterial, and tissue-repair properties [17], can enhance drug permeation through interactions with cell membranes [18], making it an effective transdermal application. Among contemporary delivery systems, microneedle (MN) technology—particularly hyaluronic acid (HA)-based soluble MNs—provides efficient, well-tolerated drug delivery for scar management [19]. These MNs provide deep skin penetration, robust mechanical strength, excellent biocompatibility [20], and intrinsic anti-scarring effects, as HA is a major component of the dermal ECM [21].

In this study, we developed an advanced therapeutic platform by coordinating Mo-based POMs ($\{Mo_{154}\}$) with EGCG to form self-assembled metal–phenolic complexes (ME_{mix}), which were subsequently co-assembled with Cs through electrostatic interactions to generate multifunctional Cs-modified ME_{mix} (CME) nanoparticles. The CME complex was then incorporated into HA-based MNs to produce CME@MN (Schemes 1a and 1b). This design exploits the synergistic effects of $\{Mo_{154}\}$ and EGCG within MPNs to simultaneously target inflammation, fibrosis, and scar-related signaling pathways while enabling efficient PTT. The co-assembly of Cs with MPNs and the MN-based transdermal delivery system addresses the intrinsic limitations of $\{Mo_{154}\}$ toxicity and poor EGCG adhesion, thereby enhancing overall biocompatibility and drug bioavailability. In this study, we aim to develop a precision delivery system capable of modulating scar-related signaling pathways through the coordinated inhibition of hyperinflammation and fibrosis, with synergistic photothermal conversion to enhance therapeutic efficacy (Scheme 1c).

2 Results and discussion

2.1 Preparation and characterization of CME

The $\{Mo_{154}\}$ anion, a giant POM with a well-defined chemical structure and a diameter of 3.4 nm, exhibits excellent water solubility and high photothermal conversion efficiency (PCE), making it highly suitable for biomedical applications [22]. Its straightforward, reproducible synthesis enables cost-effective, large-scale production. However, the clinical translation of this promising material, $\{Mo_{154}\}$, is limited by its inherent biotoxicity. To mitigate this limitation while retaining its photothermal functionality, $\{Mo_{154}\}$ was combined with EGCG, a bioactive plant polyphenol with potent free radical–scavenging, anti-inflammatory, and antibacterial properties [23]. $\{Mo_{154}\}$–EGCG nanocomposites

(ME_{mix}) were constructed using MPN chemistry [24], which not only reduces Mo_{154} toxicity but also produces synergistic effects with EGCG. Further stabilization was achieved by encapsulating ME_{mix} with Cs through electrostatic interactions, forming CME nanoparticles. This encapsulation prevents $\{Mo_{154}\}$ from binding to plasma proteins and other biomolecules, enhances biosafety, and overcomes the limited mucosal adhesion of EGCG observed in clinical applications.

The $\{Mo_{154}\}$ anion was successfully synthesized using a slightly optimized solution-phase reduction procedure based on previously reported methods [22, 25, 26]. Ultraviolet–visible (UV–Vis) spectroscopy (UV-7000, Japan) of a 50 μg/mL aqueous solution revealed a characteristic absorption peak at 750 nm (Fig. S1a in the supplementary information). Fourier-transform infrared spectroscopy (Nicolet^{TM} iS50, Germany) identified prominent peaks at 550, 630, 954, and 1610 cm^{-1} (Fig. S1b in the supplementary information), consistent with previous reports [25]. Atomic force microscopy (AFM, Bruker Multimode 8, USA) imaging confirmed a uniform spherical morphology with particle sizes of 3–4 nm (Fig. S1c in the supplementary information). Dynamic light scattering (DLS) measurements indicated monodisperse nanoparticles with an average diameter of approximately 4 nm and a zeta potential of −30.2 mV (Fig. S1d in the supplementary information). Photothermal performance under 808 nm laser irradiation revealed that the temperature of $\{Mo_{154}\}$ increased with both laser power and particle concentration. After 5 min of irradiation at 1.0 W/cm^2, the temperature reached 60 °C at 50 μg/mL (Fig. S1e in the supplementary information) and exceeded 60 °C at 100 μg/mL (Fig. S1f in the supplementary information), confirming its excellent photothermal response. Overall, comprehensive physicochemical and photothermal characterization confirmed the successful synthesis of the $\{Mo_{154}\}$ anion.

Subsequently, ME_{mix} formulations with varying Mo_{154}/EGCG mass ratios were prepared using the one-pot method (Fig. S2a in the supplementary information). Evaluation of particle size, polydispersity index (PDI), zeta potential, and photothermal performance (Table S1 and Fig. S2b in the supplementary information) supported the selection of a 1:1 mass ratio for further experiments. AFM confirmed uniform dispersion of ME_{mix} and a particle size of approximately 60 nm (Figs. S2c and S2d in the supplementary information),

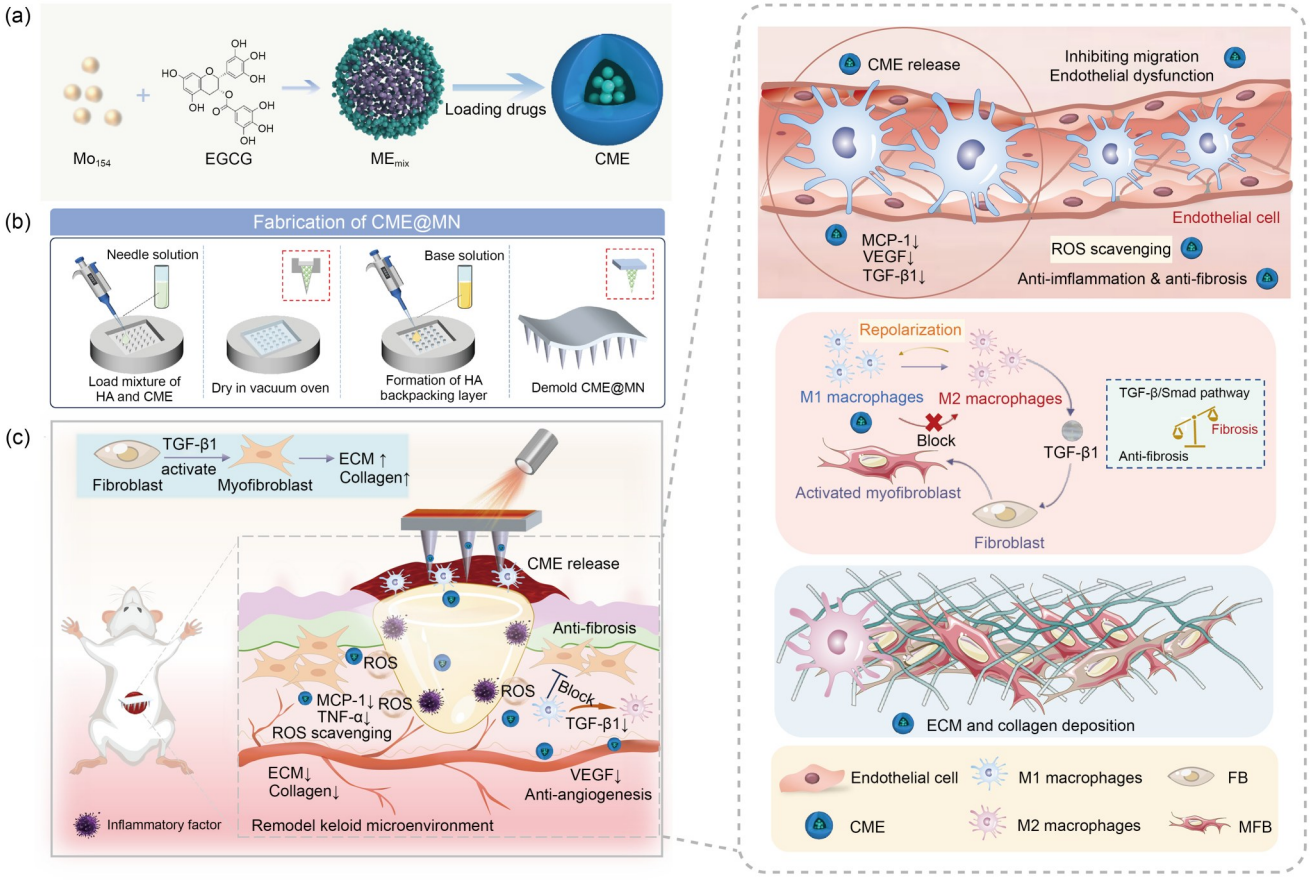

Scheme 1 Schematic illustration of the preparation of multifunctional self-assembling nanodrug CME and its synergistic application with microneedles for scar therapy, including underlying mechanisms: (a) synthesis of CME nanoparticles; (b) fabrication of CME@MN; (c) mechanism of CME@MN-mediated synergistic scar therapy and its effects on scar-related cells. FB: fibroblast; MFB: myofibroblast

consistent with DLS measurements. UV–Vis spectroscopy revealed a maximum absorption peak at 750 nm (Fig. S2e in the supplementary information).

Finally, ME_{mix} was loaded onto Cs carriers through electrostatic adsorption to generate CME nanoparticles. Screening of Cs:ME_{mix} mass ratios exhibited effective Cs coating, as indicated by the shift in zeta potential to positive values (Table S2 in the supplementary information). CME prepared at a 1:1 Cs:ME_{mix} mass ratio exhibited spherical morphology with uniform dispersion (Figs. 1a and 1b). DLS measurements showed a hydrodynamic diameter of (80.64±0.88) nm, a zeta potential of (22.13±1.21) mV, and a PDI of 0.24±0.01 (Table S2 in the supplementary information). UV–Vis spectroscopy confirmed the retention of the characteristic 750 nm absorption peak (Fig. 1c). X-ray photoelectron spectroscopy further confirmed the presence of Mo in all formulations (Fig. S3 in the supplementary information). Collectively, these results indicate successful synthesis of CME with retained {Mo_{154}} cluster-associated properties. However, the precise molecular integrity of the {Mo_{154}} cluster within the CME composite warrants further confirmation.

2.2 Physicochemical properties and biocompatibility of CME

The photothermal performance of CME was first evaluated in vitro using an infrared thermal imaging camera. The temperature of CME increased with both laser power (Fig. 1d) and nanoparticle concentration (Fig. 1e). Thermal imaging further visualized this photothermal response across varying concentrations (Fig. 1f). To balance therapeutic efficacy with the need to avoid excessive heat-induced injury to surrounding tissues, a laser power density of 1 W/cm^2 was selected for subsequent experiments. Photothermal stability was assessed through repeated irradiation cycles, which revealed negligible temperature variation across four consecutive on/off cycles (Fig. 1g), indicating strong photothermal durability. Using a well-established formula described in the literature [27], the PCE of CME was calculated to be approximately 50% (Fig. 1h). These data indicate that CME efficiently retains the photothermal characteristics associated with the {Mo_{154}} anion and highlight its potential for in vivo evaluation.

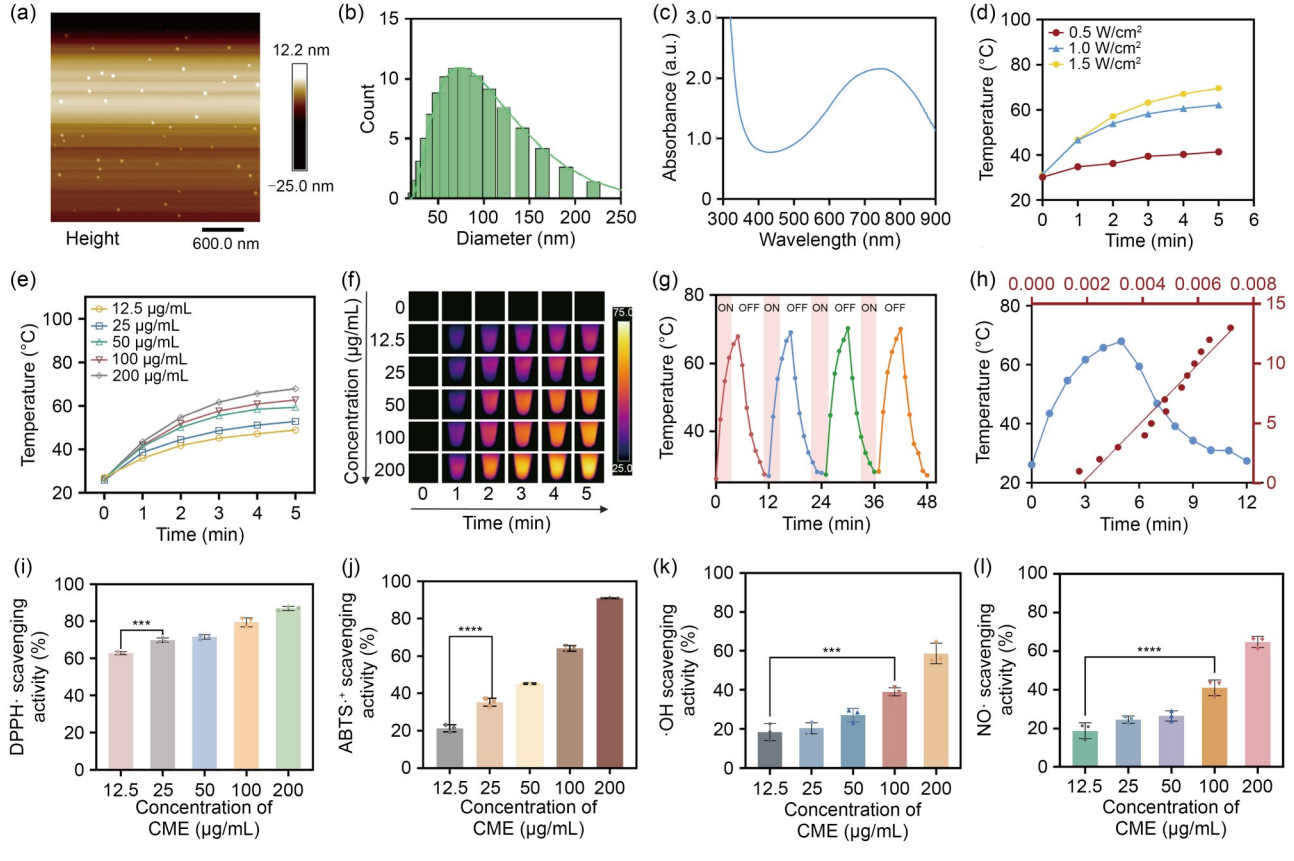

Fig. 1 Preparation and characterization of CME. (a) AFM image of the CME. (b) Corresponding particle size distribution analysis. (c) UV–Vis absorption spectrum of ME_{mix}. (d) Photothermal heating curves of CME (100 μg/mL) under 808 nm laser irradiation at different power densities. (e, f) Photothermal heating curves and corresponding infrared thermal images of CME at varying concentrations under 808 nm laser irradiation (1.0 W/cm^2). (g) Photothermal stability of CME (50 μg/mL) over four irradiation cycles (808 nm, 1.0 W/cm^2). (h) Photothermal conversion efficiency determined from cooling-phase kinetics. (i–l) The in vitro antioxidant performance of CME was identified through radical scavenging assays against DPPH· (i), $ABTS^{\cdot+}$ (j), ·OH (k), and NO· (l). Data in (i–l) are presented as mean±standard deviation (n=3). $^{***}p<0.001$ and $^{****}p<0.0001$

Solvent stability is a critical parameter for assessing pharmaceutical applicability [28]. DLS measurements over one week showed that CME maintained relatively stable hydrodynamic diameters and PDI values in water, phosphate-buffered saline (PBS, pH 7.4), Dulbecco's modified Eagle medium, and Roswell Park Memorial Institute 1640 medium for 3 d; however, pronounced aggregation was observed by Day 5 (Fig. S4 in the supplementary information).

Persistent inflammatory activity during wound healing can contribute to excessive scar formation. Antioxidant interventions can help modulate ROS-mediated inflammatory pathways and thereby suppress pathological scarring [29]. The antioxidant performance of CME was evaluated across multiple radicals, exhibiting concentration-scavenging effects on the 1,1-diphenyl-2-picrylhydrazyl radical (DPPH·) (Fig. 1i), 2,2'-azino-bis (3-ethylbenzothiazoline-6-sulfonic acid) radical ($ABTS^{\cdot+}$) (Fig. 1j), hydroxyl radical (·OH) (Fig. 1k), and nitric oxide (NO·) (Fig. 1l). At 100 μg/mL, CME showed scavenging efficiency of 80% for DPPH·, 64% for $ABTS^{\cdot+}$, 40% for ·OH, and 42% for NO·, indicating substantial antioxidant activity that may contribute to mitigating inflammation-associated scarring.

Given the straightforward synthesis and strong biocompatibility of MPNs in mitigating metal ion-associated toxicity [30], we assessed whether CME reduces the cytotoxicity of $\{Mo_{154}\}$. Cytotoxicity of $\{Mo_{154}\}$ was first evaluated in normal human skin fibroblasts (HSF) and human immortalized keratinocytes (HaCat) using 3-(4,5-dimethylthiazol-2-yl)-2,5-diphenyltetrazolium bromide (MTT) assays (Fig. S5a in the supplementary information). $\{Mo_{154}\}$ significantly inhibited HSF and HaCat proliferation, with further reductions in viability following photothermal irradiation, consistent with its strong photothermal ablation effect. Treatment with ME_{mix} improved cell viability (Fig. S5b in the supplementary information), supporting the role of the MPN strategy in enhancing biosafety. CME exhibited minimal cytotoxicity in HSF, maintaining approximately 75% cell viability, even at 200 μg/mL after 24 h of incubation with laser irradiation (Fig. S6a in the supplementary information). Live/Dead cell staining further confirmed that MPN formation and Cs encapsulation substantially decreased $\{Mo_{154}\}$-associated toxicity (Fig. S6b in the supplementary information).

Hemocompatibility was further assessed using a hemolysis assay (Fig. S7 in the supplementary information). CME exhibited minimal hemolytic activity, with hemolysis rates remaining below 5% at concentrations up to 200 μg/mL, indicating excellent blood compatibility suitable for in vivo applications.

By rationally engineering the MPN structure, CME integrates exceptional photothermal performance, potent antioxidant activity, stable colloidal properties, and high biocompatibility. These multifunctional attributes position CME as a promising platform for HS therapy through synergistic photothermal and antioxidative mechanisms.

2.3 Fabrication and characterization of CME@MN

HSs result from aberrant tissue repair following dermal or deep tissue injury [31]. Despite advances in HS management, current therapies have not consistently achieved optimal clinical outcomes, primarily due to excessively thick, rigid scar tissue that exacerbates skin barrier dysfunction and hinders effective drug penetration and release. MN technology has emerged as a promising transdermal delivery platform for HS therapy, enabling direct skin implantation, stimulating ECM remodeling, and reducing tissue stress [32]. To enhance anti-scarring efficacy through synergistic mechanisms, CME was incorporated into dissolvable HA MNs, hereafter designated as CME@MN.

CME@MN was fabricated using a polydimethylsiloxane mold and characterized through stereomicroscopy (Fig. S8 in the supplementary information), featuring a 15×15 array of conical MNs with uniform morphology and distribution (Fig. 2a). Scanning electron microscopy (SEM; Hitachi SU-70, Japan) revealed well-defined MN structures with consistent dimensions (approximately 800 μm in height and 300 μm in base width; Fig. 2b). Mechanical testing using a universal tensile testing machine showed a maximum fracture force of 0.39 N (Fig. 2c), exceeding the 0.045 N threshold required for skin penetration, indicating sufficient mechanical strength for transdermal delivery. Ex vivo experiments on porcine skin showed complete dissolution of CME@MN after application (Fig. 2d), leaving uniform micropores (Fig. S9 in the supplementary information), indicative of efficient penetration and drug release.

The drug-loading capacity of CME@MN was quantified using absorbance measurements against a CME standard curve (Fig. S10 in the supplementary information), yielding (73.63±0.82) μg per patch. Laser therapy, a standard adjuvant for scar treatment, enables deep tissue penetration and facilitates photothermal decomposition and remodeling of collagen through collagen regeneration [33]. To confirm that CME retained its photothermal activity after MN incorporation, the photothermal performance of CME@MN was systematically assessed using an infrared thermal imager (Fig. 2e). Compared with blank MNs (Blank MN), $\{Mo_{154}\}$-loaded MNs (Mo_{154}@MN), ME_{mix}-loaded MNs (ME_{mix}@MN), and CME@MN exhibited remarkable photothermal responsiveness. Under 808 nm laser irradiation (1.0 W/cm^2, 5 min), CME@MN reached 61.2 °C, which is intermediate between Mo_{154}@MN (67.1 °C) and ME_{mix}@MN (58.6 °C), with all exceeding the 45 °C threshold required for effective PTT. These results confirm that CME@MN maintains superior photothermal characteristics suitable for therapeutic applications. Drug release kinetics, assessed using Franz diffusion cells (Fig. 2f), showed approximately 80% cumulative release over 24 h (Fig. 2g), indicating sustained delivery,

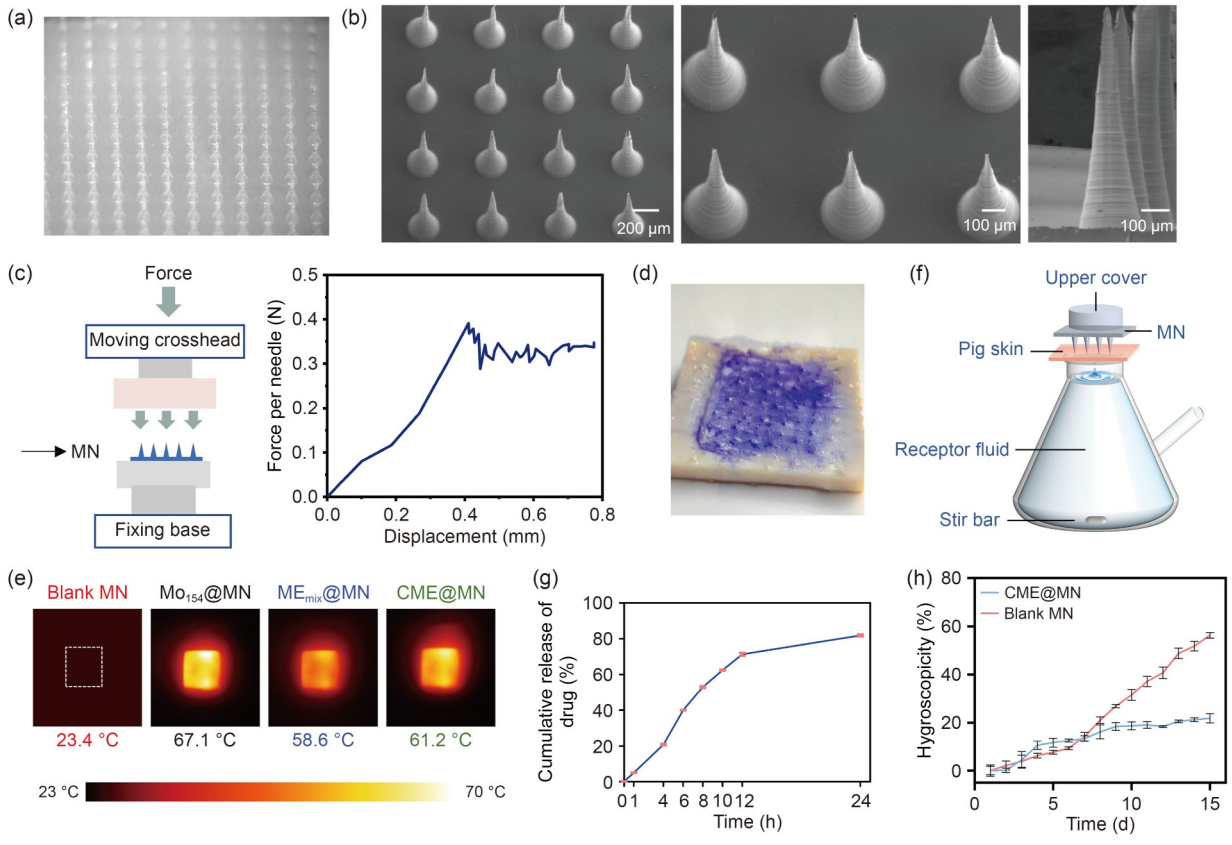

Fig. 2 Fabrication and characterization of CME@MN. (a) Macroscopic morphology of CME@MN arrays. (b) SEM images showing the detailed morphology of CME@MN. (c) Schematic illustration of the mechanical testing setup and corresponding mechanical strength analysis of CME@MN. (d) Evaluation of the skin penetration capability of CME@MN using an ex vivo porcine skin model. (e) Photothermal conversion performance of various MN patches under 808 nm laser irradiation (1.0 W/cm^2, 5 min). (f) Schematic illustration of the modified Franz diffusion cell system for transdermal drug release studies. (g) Drug release profile of CME@MN. (h) Hygroscopicity of CME@MN under storage conditions. Data in (g, h) are presented as mean±standard deviation (n=3)

which is essential for prolonged therapeutic action. Stability assessments showed negligible changes in the hygroscopicity of CME@MN over 15 d of storage at ambient temperature, whereas the Blank MN group exhibited significant hygroscopic variation (Fig. 2h), confirming the enhanced stability of CME@MN under routine storage conditions.

2.4 Cellular uptake and deep penetration in keloid fibroblasts

HSs develop through aberrant tissue repair, characterized histopathologically by hyperproliferation of fibroblasts, excessive deposition of ECM components—particularly collagen—and pathological neovascularization [34]. Effective fibroblast targeting and suppression are therefore critical strategies for scar intervention. Since the efficacy of nanomedicine largely depends on cellular internalization efficiency, we first assessed CME uptake in human keloid fibroblasts (HKF). Flow cytometry revealed time-dependent CME internalization in HKF cells (Fig. 3a), with detectable signals at 30 min and saturation at 4 h. These findings were corroborated by confocal laser scanning microscopy (CLSM, Leica TCS SP8, Germany) (Fig. 3b). The rapid uptake likely stems from the favorable physicochemical properties of CME, including its small particle size and optimal surface characteristics that enhance cellular penetration.

Subcellular localization studies showed preferential accumulation of CME in the mitochondria (Fig. 3c). Quantitative analysis of fluorescence co-localization using ImageJ revealed substantial overlap between CME (red) and MitoTracker green signals, with higher Pearson correlation coefficients than those observed with lysosomal markers. Given the central metabolic role of mitochondria and the established association between mitochondrial stress and keloid fibroblast apoptosis [35], these results suggest that CME may induce apoptosis through mitochondrial-mediated pathways in these key scar-forming fibroblasts.

Compared with normal skin, HSs exhibit epidermal thickening, collagen fiber densification, and disorganized ECM architecture, which substantially impede drug penetration and diffusion [36]. To assess the transdermal penetration efficiency of CME, four formulations—{Mo_{154}}, ME_{mix},

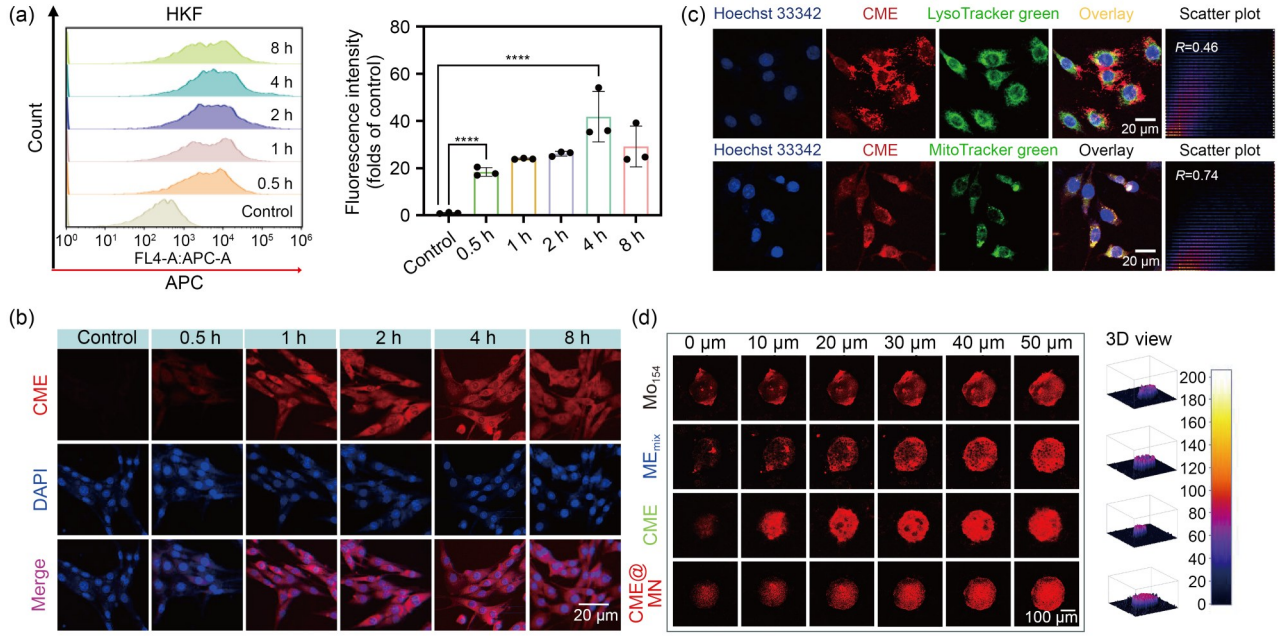

Fig. 3 Cellular uptake and penetration capacity of CME in HKF. (a) Time-course flow cytometry analysis of CME uptake in HKF, with quantitative assessment of the relative mean fluorescence intensity. (b) CLSM images showing CME uptake by HKF cells (scale bar: 20 μm). (c) Subcellular localization of CME in HKF (scale bars: 20 μm). (d) CLSM images and corresponding 3D surface plots at 50 μm depth showing the penetration efficiency of different formulations in HKF spheroids (scale bar: 100 μm). Data in (a) are presented as mean±standard deviation (n=3). $^{****}p<0.0001$

CME, and CME@MN—were tested using three-dimensional (3D) HKF spheroids, which model the HS-like tissue barrier. Depth-resolved confocal imaging and 3D surface plot analysis at 50 μm depth revealed markedly enhanced penetration of CME formulations (Fig. 3d), with strong fluorescence signals in the spheroid cores. This improved penetration profile is likely mediated by the Cs component of CME, which facilitates tissue permeation through its known penetration-enhancing properties. These findings highlight the potential of CME, particularly when delivered through MN systems, for efficient transdermal targeting of deep scar tissue.

2.5 Therapeutic suppression of keloid fibrosis by CME

To evaluate the regulatory effects of CME on HKF cells, its anti-proliferative activity was assessed using MTT assays. As shown in Fig. 4a, CME inhibited HKF cell proliferation in a dose-dependent manner. Photothermal stimulation with 808 nm laser irradiation further decreased cellular viability, with near-complete cell death observed at higher CME concentrations combined with laser treatment. Comparative analysis with ME_{mix} (Fig. S11 in the supplementary information) revealed that CME exerts more potent inhibitory effects, underscoring its enhanced anti-fibrotic potential. Notably, extending the incubation period to 48 h (Fig. S12a in the supplementary information) produced cytotoxicity comparable to the 24 h treatment, suggesting rapid pharmacological action. Furthermore, CME exhibited selective toxicity toward HKF compared with normal HSF (Fig. S6a in the supplementary information), which correlated with substantially higher cellular uptake in HKF (Fig. S12b in the supplementary information). This selective activity toward keloid fibroblasts underscores the potential of CME as a targeted therapeutic agent for the management of hypertrophic and keloid scars.

Excessive oxidative stress often triggers sustained inflammatory responses, driving fibroblast hyperactivation and pathological ECM overproduction during early-stage scar formation, thereby promoting fibrotic progression [37]. Targeting oxidative stress is therefore a strategic approach for early scar intervention. To evaluate the regulatory effects of CME on oxidative stress, intracellular ROS levels in HKF cells were quantified post-treatment using flow cytometry (Figs. 4b and 4c) and CLSM (Fig. 4d). All tested formulations ({Mo_{154}}, ME_{mix}, and CME) significantly reduced green fluorescence intensity, indicating endogenous ROS scavenging. Notably, photothermal irradiation further enhanced the ROS-scavenging capacity of all treatment groups, with CME exhibiting the most potent effect. These findings show that CME can effectively restore redox homeostasis in the scar microenvironment, representing a promising approach to preventing pathological fibrosis.

Excessive collagen fiber deposition and ECM accumulation are hallmark pathological features of HSs. Masson's

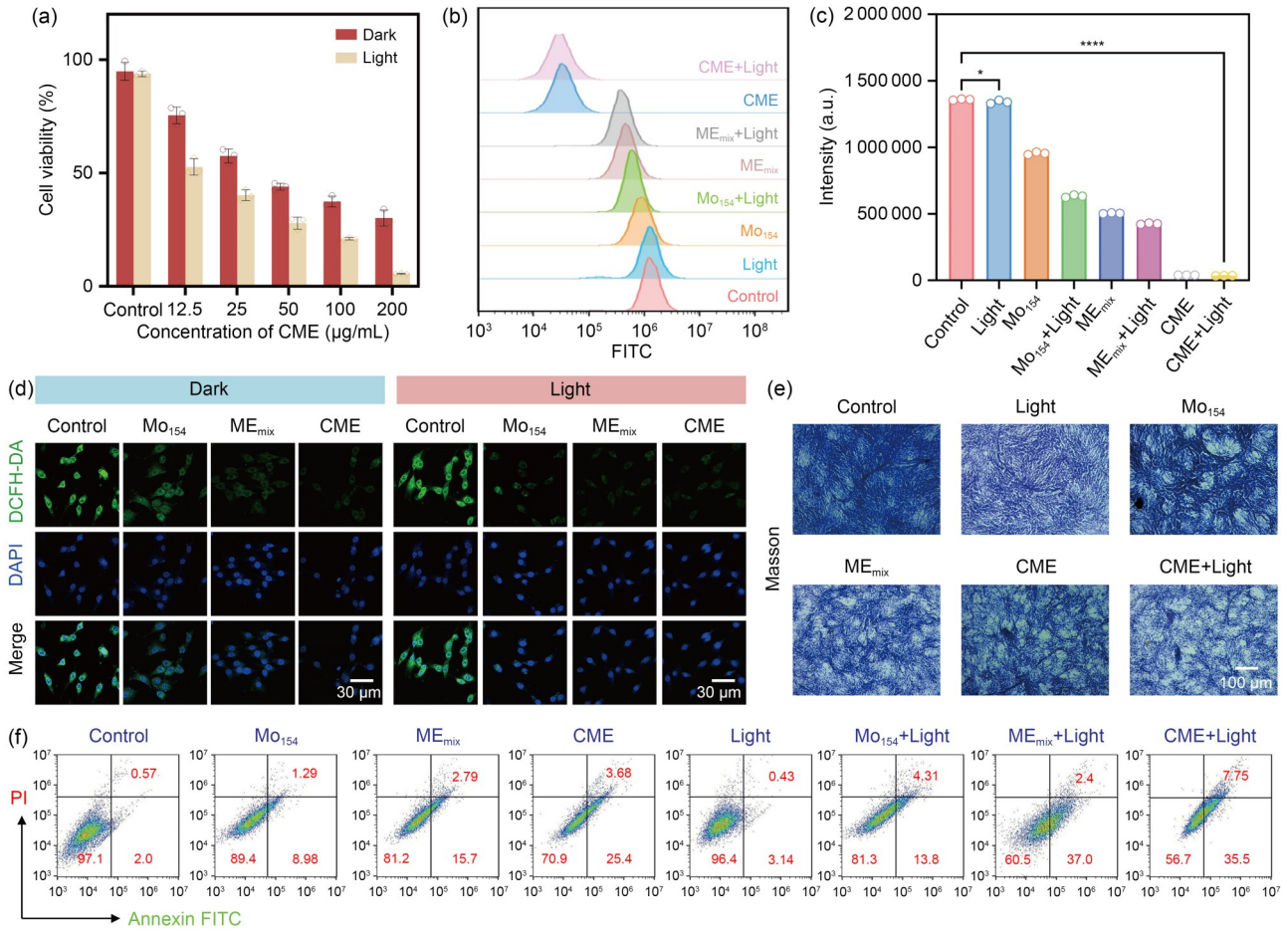

Fig. 4 Effects of CME on HKF activity. (a) Anti-proliferative effects of CME on HKF. (b, c) Flow cytometry histograms and quantitative analysis of intracellular ROS levels in HKF following different treatments. (d) CLSM visualization of intracellular ROS levels in HKF (scale bars: 30 μm). (e) Masson's trichrome staining of HKF to assess ECM and collagen deposition (scale bar: 100 μm). (f) Flow cytometry detection of apoptosis in HKF. Data in (a, c) are presented as mean±standard deviation (n=3). $^{*}p<0.05$ and $^{****}p<0.0001$

trichrome staining, which differentiates collagen fibers (blue, aniline blue), muscle fibers (red, acid fuchsin), and nuclei (black, hematoxylin), was used to evaluate ECM modulation (Fig. 4e). The control samples exhibited intense blue staining, indicating abundant collagen deposition. All treatment groups showed reduced blue intensity, reflecting decreased ECM production. Notably, CME showed superior collagen suppression compared with {Mo_{154}} and ME_{mix}, and photothermal irradiation further enhanced the ECM-inhibitory effect across all groups. Collectively, these results indicate that CME effectively reduces pathological collagen fiber accumulation, attenuates excessive ECM deposition, and remodels the fibrotic scar microenvironment.

To evaluate the apoptotic effects of CME on HKF cells, Annexin V–fluorescein isothiocyanate (FITC) conjugate and propidium iodide staining were performed, followed by flow cytometric analysis (Fig. 4f). All tested formulations ({Mo_{154}}, ME_{mix}, and CME) induced apoptosis, with photothermal treatment further enhancing this response. CME combined with laser irradiation produced the highest apoptosis rate. These results indicate that CME effectively penetrates fibrotic scar tissue, potently scavenges intracellular ROS, synergizes with PTT to inhibit pathological ECM accumulation, facilitates collagen remodeling, and ultimately induces apoptosis in HS fibroblasts.

2.6 Regulation of endothelial migration and secretory function by CME

During the proliferative phase of HS, vascular endothelial cells undergo active proliferation and migration to support fibroblast expansion by supplying nutrients to the developing scar tissue [38]. These endothelial cells also directly secrete profibrotic cytokines, including VEGF and TGF-β1, which contribute to fibroblast activation. To evaluate whether CME modulates these endothelial behaviors, we examined its effects on human umbilical vein endothelial cell (HUVEC) uptake, proliferation, migration, and cytokine secretion.

Flow cytometry (Fig. 5a; Fig. S13 in the supplementary information) and CLSM imaging (Fig. 5b) confirmed efficient

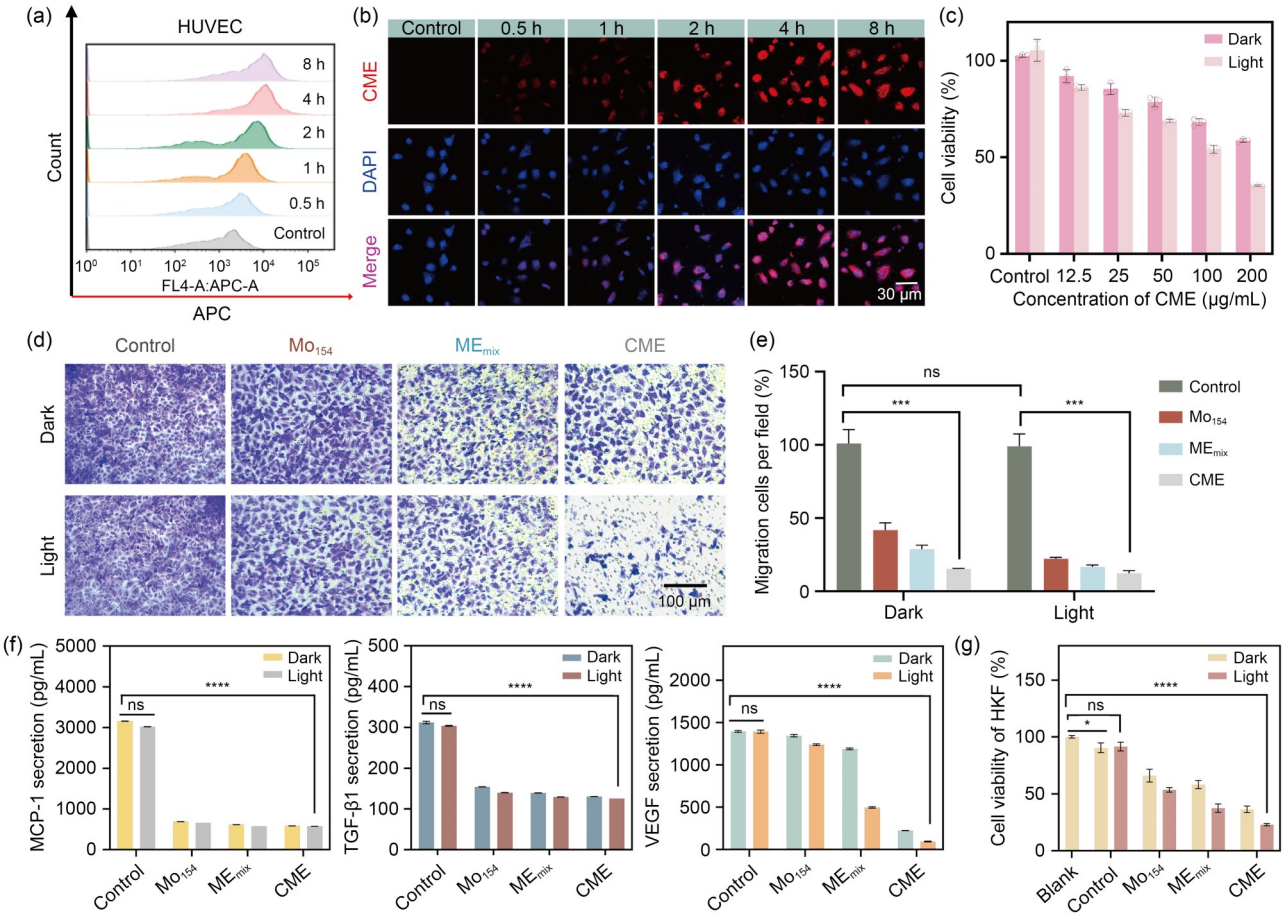

Fig. 5 Effects of CME on the proliferation, migration, and secretory functions of HUVECs. (a) Kinetics of CME internalization in HUVECs analyzed by flow cytometry. (b) CLSM visualization of CME uptake in HUVECs (scale bar: 30 μm). (c) Dose-dependent anti-proliferative effects of CME on HUVECs after 24 h of treatment. (d) Transwell migration assay images (scale bar: 100 μm). (e) Quantitative analysis of HUVEC migration after different treatments. (f) MCP-1, TGF-β1, and VEGF levels in HUVEC culture supernatants after treatment. (g) HKF proliferation in response to conditioned media derived from HUVECs after 24 h of culture. Data in (c, e–g) are presented as mean±standard deviation (n=3). $^{*}p<0.05$, $^{***}p<0.001$, and $^{****}p<0.0001$; ns: not significant

CME internalization by HUVECs. Subsequent MTT assays revealed that CME reduced HUVEC proliferation in a dose-dependent manner (Fig. 5c), and this effect was inhibited under 808 nm laser irradiation. Extending the treatment to 48 h strengthened this suppression (Fig. S14 in the supplementary information). When compared with ME_{mix} (Fig. S15 in the supplementary information), CME exhibited superior inhibitory activity, highlighting its potent anti-angiogenic properties, which are critical for targeting the pathological blood vessels and fibrotic overgrowth in HSs.

Given that vascular endothelial cells secrete multiple cytokines that contribute to HS formation and that endothelial dysfunction is known to suppress fibroblast proliferation [39], we further examined the regulatory role of CME by assessing its effects on HUVEC migration and cytokine secretion. Treatment with {Mo_{154}}, ME_{mix}, and CME substantially reduced HUVEC migration, and this reduction was enhanced by photothermal treatment (Figs. 5d and 5e). CME combined with laser irradiation produced the greatest inhibition of migration. Enzyme-linked immunosorbent assay (ELISA) of conditioned media revealed significant downregulation in profibrotic cytokines MCP-1, TGF-β1, and VEGF across all treatment groups (Fig. 5f), indicating that CME suppresses HUVEC secretory activity. Notably, the photothermal effect specifically enhanced VEGF inhibition without altering MCP-1 or TGF-β1 suppression.

Fibroblasts and vascular endothelial cells play interdependent roles in scar formation. In co-culture experiments, conditioned media from treated HUVECs revealed that supernatants from {Mo_{154}}-, ME_{mix}-, and CME-treated cells inhibited HKF proliferation (Fig. 5g). Collectively, these findings indicate that CME regulates scar fibroblast activity by inhibiting HUVEC migration and cytokine secretion, thereby reducing inflammatory signaling through MCP-1 downregulation and disrupting nutrient supply to fibroblasts through VEGF/TGF-β1 suppression. This combined targeting of endothelial and fibrotic pathways suggests that CME has therapeutic potential for the management of HS.

2.7 Modulation of THP-1 macrophage polarization by CME

Macrophages contribute significantly to HS pathogenesis by secreting cytokines that promote fibrosis and cell proliferation. M2 macrophage infiltration is a hallmark of scar tissues, where these cells drive fibroblast-to-myofibroblast differentiation and fibrotic progression through TGF-β1 secretion. To assess the immunomodulatory effects of CME, we examined its influence on macrophage polarization in human monocytic leukemia THP-1 cells. Notably, THP-1 cells were first differentiated into M0 macrophages (THP-1-M0) using phorbol 12-myristate 13-acetate (100 ng/mL).

Flow cytometry (Fig. 6a; Fig. S16 in the supplementary information) and CLSM imaging (Fig. 6b) confirmed the rapid and efficient cellular uptake of CME nanoparticles by THP-1-M0 macrophages. Cytotoxicity was assessed using MTT assays (Fig. 6c; Fig. S17 in the supplementary information),

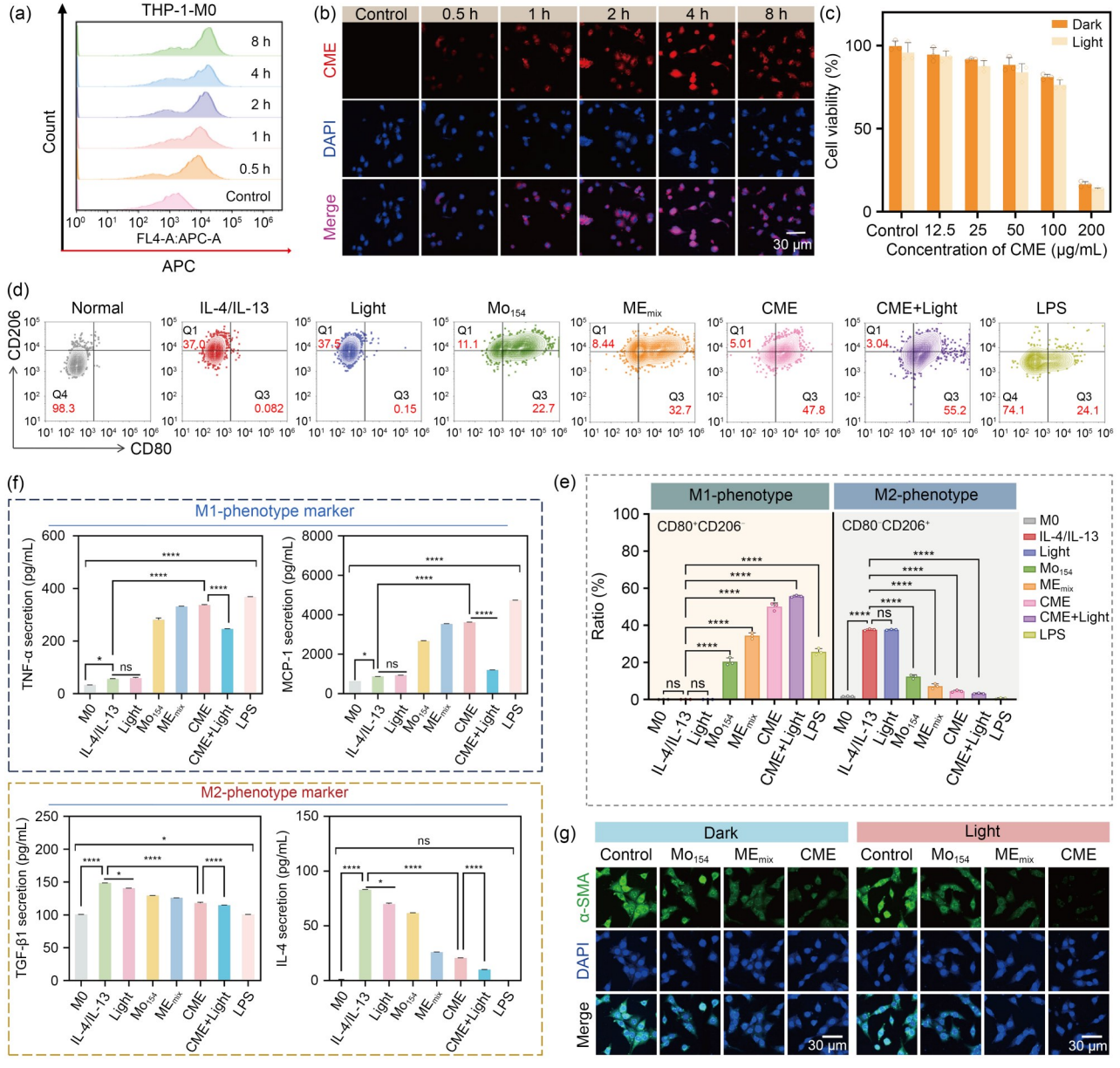

Fig. 6 CME-mediated modulation of THP-1-M0 macrophage activity. (a) Flow cytometric analysis of CME uptake by THP-1-M0 cells. (b) CLSM images showing cellular internalization of CME in THP-1-M0 cells (scale bar: 30 μm). (c) Anti-proliferative effects of CME on THP-1-M0 cells after 24 h of treatment. (d) Flow cytometric analysis of macrophage polarization using M1 (CD80-Allophycocyanin) and M2 (CD206-Phycoerythrin) surface markers through double staining. (e) Quantitative analysis of macrophage polarization based on flow cytometry data. (f) Levels of TNF-α, MCP-1, TGF-β1, and IL-4 in THP-1-M2 cell culture supernatants following different treatments. (g) Immunofluorescence detection of α-SMA expression in HKF cells cultured with M2 macrophage-conditioned medium (green: α-SMA; scale bars: 30 μm). Data in (c, e, f) are presented as mean±standard deviation (n=3). $^{*}p<0.05$ and $^{****}p<0.0001$; ns: not significant. LPS: lipopolysaccharide

which showed favorable biocompatibility, with cell viability exceeding 80% at concentrations below 100 μg/mL after 24 h. CME also exhibited significantly lower cytotoxicity than ME_{mix} under equivalent dosing conditions (Fig. S18 in the supplementary information). Moreover, CME exerted minimal effects on THP-1-M0 macrophages compared with its more potent inhibitory activity in HUVECs and HKF cells, highlighting its selective anti-fibrotic and anti-angiogenic properties, as well as its therapeutic potential for HS treatment.

Given the pivotal role of M2 macrophages in promoting fibroblast activation [40], we evaluated the regulatory effects of CME on THP-1 macrophage polarization. Surface marker expression was first assessed using flow cytometry (Fig. 6d). Lipopolysaccharide (LPS) stimulation significantly upregulated M1 marker CD80 expression while maintaining stable CD206 levels in THP-1-M0 cells, confirming successful M1 polarization. Conversely, interleukin-4/interleukin-13 (IL-4/IL-13) treatment markedly elevated the expression of the M2 marker CD206 without affecting CD80 expression, indicating effective M2 differentiation. Flow cytometric analysis of polarized M2 macrophages (24 h post-treatment) identified distinct $CD80^{-}CD206^{+}$ (Q1, M2 phenotype) and $CD80^{+}CD206^{-}$ (Q3, M1 phenotype) subpopulations (Fig. 6e). CME treatment significantly reduced the Q1 population while increasing Q3 proportions compared to $\{Mo_{154}\}$ and ME_{mix} controls, indicating that CME effectively reprograms macrophage polarization from a profibrotic M2 phenotype toward a proinflammatory M1 phenotype. This reprogramming effect was further enhanced by NIR irradiation.

We next quantified M1-associated secreted factors (tumor necrosis factor-α (TNF-α) and MCP-1) and M2-associated secreted factors (IL-4 and TGF-β1) in culture supernatants from each treatment group using ELISA (Fig. 6f). The results were consistent with the flow cytometry findings. LPS stimulation increased M1-associated cytokine secretion, while IL-4/IL-13 stimulation enhanced the secretion of M2-associated markers. Treatment with $\{Mo_{154}\}$, ME_{mix}, and CME increased M1-associated cytokine secretion while simultaneously reducing M2-associated cytokine secretion, indicating that CME influences a shift in macrophage polarization from an M2 phenotype toward an M1 phenotype. However, an exception was observed in the CME+Light group, in which M2-associated cytokine secretion was suppressed, as expected, but M1-associated cytokine secretion was also reduced. This outcome may reflect laser-induced modulation of macrophage function or altered metabolism under photothermal stimulation [41].

To further confirm that CME promotes the repolarization of M2 macrophages toward the M1 phenotype and inhibits fibroblast activation, HKF cells were co-cultured with supernatants derived from THP-1-M2 cells treated with $\{Mo_{154}\}$, ME_{mix}, or CME for 24 h. The degree of activation of HKF cells was evaluated using the fibroblast marker α-SMA. Immunofluorescence imaging (Fig. 6g) showed a progressive decrease in α-SMA fluorescence in HKF cells exposed to conditioned media from $\{Mo_{154}\}$-, ME_{mix}-, or CME-treated THP-1-M2 macrophages. These results indicate that $\{Mo_{154}\}$, ME_{mix}, and CME promote M2-to-M1 macrophage repolarization, which in turn significantly inhibits fibroblast activation and attenuates fibrotic activity, ultimately supporting the therapeutic potential of CME for pathological scar formation.

2.8 In vivo biodistribution and photothermal effect of CME@MN

In the established murine HS model (Fig. 7a), MN penetration was first evaluated. Following the CME@MN application, microscopic pores were observed in the HS tissue. Subsequent crystal violet staining revealed extensive dye diffusion, confirming effective tissue permeation (Fig. S19a in the supplementary information). Furthermore, strong fluorescence signals were observed throughout the frozen skin sections (Fig. S19b in the supplementary information), indicating efficient MN penetration and successful drug release.

Biodistribution of CME@MN was further assessed using NIR fluorescence imaging (λ_{em}=750 nm). Following the MN application, the dissolvable matrix facilitated the rapid release of CME into the scar tissue, resulting in a time-dependent increase in fluorescence intensity at the lesion site, with maximal drug accumulation evident within 24 h (Fig. 7b), confirming the capacity of CME@MN for precise delivery and sustained release. Notably, residual fluorescence persisted in the CME@MN group 72 h after patch removal (Fig. S20 in the supplementary information), indicating prolonged drug retention at the target site.

Systemic metabolic kinetics were assessed through in vivo fluorescence imaging. Within 0.5–1.0 h post-administration, fluorescence signals were predominantly localized in metabolic organs (liver>kidney>spleen>bladder). By 4 h, the residual signal persisted only in the liver, with complete elimination observed within 24 h (Fig. 7c). This favorable biodistribution profile, characterized by transient hepatic accumulation followed by efficient urinary excretion, indicates the biosafety of CME.

Infrared thermographic analysis revealed distinct photothermal responses among the treatment groups under NIR irradiation (808 nm, 1.0 W/cm^2) (Fig. 7d). All metal-containing MN formulations (Mo_{154}@MN, ME_{mix}@MN, and CME@MN) exhibited significant temperature elevation at scar sites, with temperature differentials following the hierarchy Mo_{154}@MN>CME@MN>ME_{mix}@MN (Fig. 7e). Conversely, no significant temperature change was detected in the PBS and EGCG@MN control groups, which fully confirmed the excellent PCE of the metal-containing formulations.

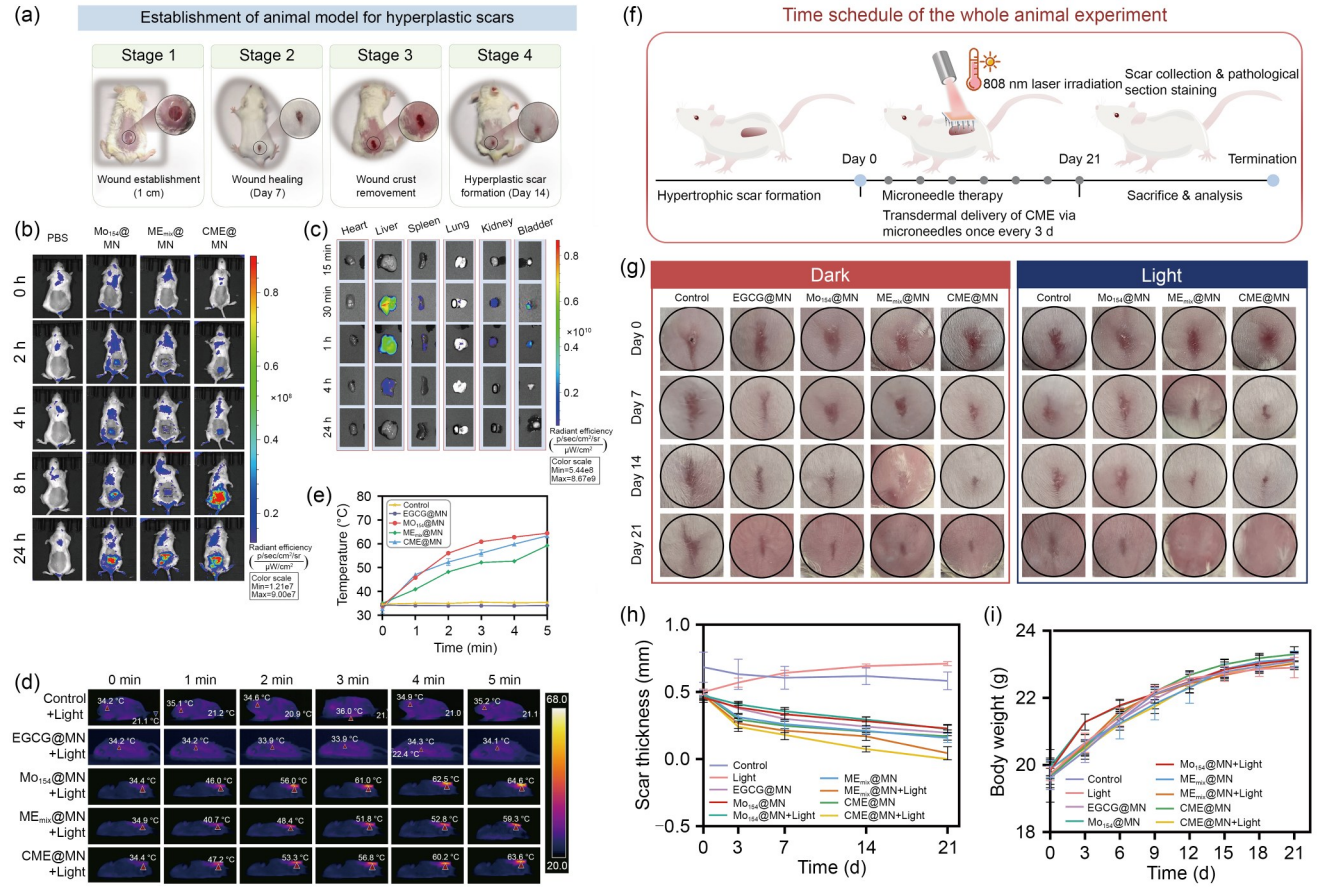

Fig. 7 In vivo biodistribution and therapeutic efficacy of CME@MN in a murine model with HS. (a) Schematic illustration of dorsal HS induction. (b) Time-dependent biodistribution of CME following MN patch administration, monitored through in vivo fluorescence imaging. (c) Ex vivo fluorescence imaging showing the organ-specific distribution of CME after intraperitoneal injection at specified time points. (d) Infrared thermal images of HS mice under 808 nm laser irradiation (1 W/cm^2) across treatment groups. (e) Quantitative analysis of temperature changes in scar tissue during laser irradiation. (f) Therapeutic protocol for combined CME@MN transdermal delivery and PTT. (g) Representative images documenting scar progression during the treatment period. (h) Monitoring scar thickness across treatment groups. (i) Changes in body weight during the treatment course. Data in (e, h, i) are presented as mean±standard deviation (n=5)

2.9 In vivo anti-scar efficacy and biosafety of CME@MN

The therapeutic efficacy of CME@MN was evaluated in a murine HS model, with EGCG@MN serving as a positive control. MN patches (EGCG@MN, Mo_{154}@MN, ME_{mix}@MN, and CME@MN) were locally administered every 3 d for 21 d, combined with 808 nm NIR laser-triggered PTT (Fig. 7f). The 3-d dosing interval was determined based on in vivo biodistribution data (Fig. 7b; Fig. S20 in the supplementary information), which revealed persistent CME accumulation at the scar site for over 24 h. This prolonged retention suggests a potential reservoir effect, supporting sustained local drug availability. The 3-d regimen was therefore selected to maintain therapeutic efficacy while minimizing application frequency and enhancing practical usability. The untreated model group exhibited typical HS characteristics, including epidermal thickening, hyperpigmentation, and tissue hardening (Fig. 7g). Conversely, all treatment groups showed progressive scar lightening and softening, with the most pronounced improvement observed in the CME@MN group combined with laser irradiation. Among the other treatments, ME_{mix}@MN exhibited greater scar regression than Mo_{154}@MN and EGCG@MN, whereas Mo_{154}@MN and EGCG@MN showed no significant difference in efficacy (Fig. 7g).

Physiological parameters and scar thickness were monitored throughout the treatment period. Scar thickness decreased significantly in all MN-treated groups (EGCG@MN, Mo_{154}@MN, ME_{mix}@MN, and CME@MN), with the most significant decrease observed in groups receiving adjunctive PTT (Fig. 7h). No behavioral abnormalities or body weight fluctuations were detected in any group (Fig. 7i). These findings underscore the substantial therapeutic potential of CME@MN combined with PTT for HS management, particularly given its shorter treatment duration (21 d) compared to conventional approaches such as silicone patch (3–6 months) or subcutaneous steroid injections (4–6 months) [29, 42].

To further assess the anti-scar efficacy of CME@MN, histological analyses of scar tissues were performed for each treatment group (Fig. 8a). The control samples exhibited marked epidermal hyperplasia, loss of basal spinous processes, inflammatory cell infiltration, and disorganized collagen fibers. Phototherapy alone (Light group) produced negligible improvement, while all MN-treated groups exhibited reduced inflammation and improved tissue architecture, with photothermal treatment further decreasing inflammatory cell infiltration. The therapeutic effect followed the hierarchy: Mo_{154}@MN<ME_{mix}@MN<CME@MN. Notably, the CME@MN+Light group achieved near-normal epidermal thickness, restoration of dermal appendages (e.g., sweat glands and hair follicles), orderly collagen alignment, and complete inhibition of inflammation.

Sirius Red staining confirmed excessive collagen deposition in untreated scars (Fig. 8b). Phototherapy alone did not significantly alter collagen density, whereas MN treatments (EGCG@MN, Mo_{154}@MN, ME_{mix}@MN, and CME@MN) markedly reduced fibrosis. Adjunctive PTT further enhanced collagen decomposition. Quantitative analysis revealed that the CME@MN+Light group exhibited the most significant reduction in fibrosis (Fig. 8c), indicating that CME@MN effectively alleviates HS progression by regulating collagen metabolism.

Chronic inflammation drives pathological scar formation by dynamically regulating immune cells and inflammatory mediators. TGF-β1, a key effector secreted by M2 macrophages, promotes abnormal collagen synthesis and deposition [43]. VEGF supplies nutrients to fibroblasts, and its high expression exerts profibrotic effects [44]. Analysis of cytokine expression profiles via ELISA (Fig. 8d) revealed that CME@MN significantly modulates the inflammatory and fibrotic microenvironment. CME@MN exerted potent anti-fibrotic activity by downregulating VEGF and TGF-β1 expression. Prior to laser irradiation, TNF-α and MCP-1 levels

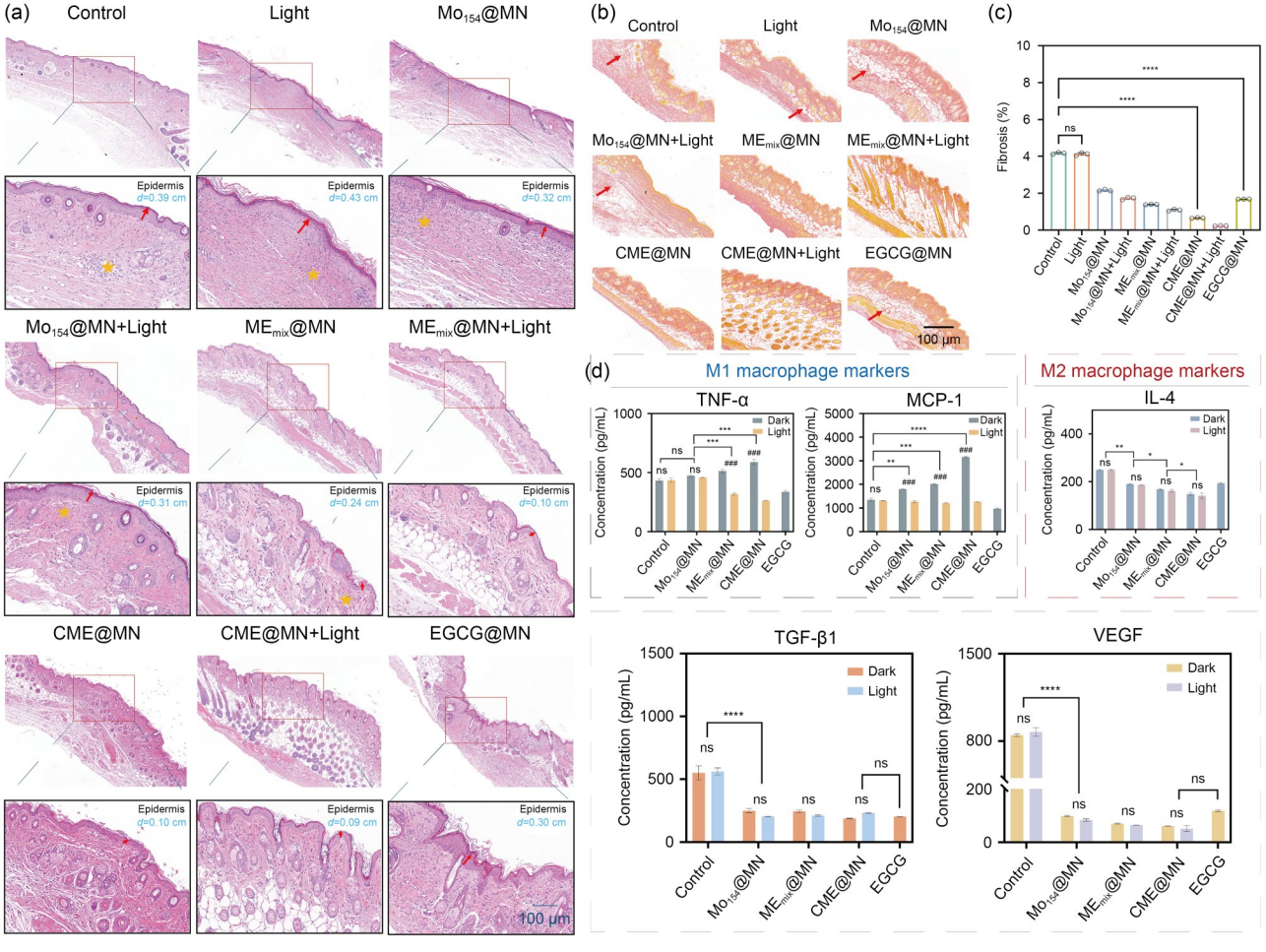

Fig. 8 Anti-inflammatory and anti-fibrotic mechanisms of CME@MN in scar treatment. (a) Histopathological assessment of scar tissues using H&E staining (scale bar: 100 μm; red arrows indicate epidermis; yellow stars denote inflammatory cell infiltration). (b, c) Sirius Red staining of collagen deposition analysis (red arrows denote collagen fibers; scale bar: 100 μm) with corresponding quantitative analysis of fibrosis severity. (d) Cytokine expression profiles (TNF-α, MCP-1, IL-4, TGF-β1, and VEGF) in scar tissues across treatment groups. Data in (c, d) are presented as mean±standard deviation (n=3). $^{*}p<0.05$, $^{**}p<0.01$, $^{***}p<0.001$, and $^{****}p<0.0001$; ns: not significant. $^{\#\#\#}p<0.001$ compared with each corresponding light group

were elevated, while IL-4 expression was slightly reduced, reflecting M2-to-M1 macrophage polarization that favors anti-fibrotic activity. However, following PTT, TNF-α expression and MCP-1 expression were markedly suppressed, consistent with in vitro observations, potentially due to laser-mediated macrophage functional reprogramming or metabolic adaptation [41]. Overall, Mo_{154}@MN, ME_{mix}@MN, and CME@MN promote M2-to-M1 macrophage polarization, thereby enhancing anti-fibrotic efficacy, while PTT effects provide complementary anti-inflammatory benefits through inflammatory cytokine suppression. Collectively, these dual mechanisms act synergistically to produce the observed robust anti-scarring efficacy of these materials.

These results suggest that CME@MN exerts an anti-scar effect through two complementary mechanisms: immunomodulation of macrophage polarization and direct inhibition of fibrotic pathways. The PTT effect substantially enhances these therapeutic outcomes by reshaping the inflammatory microenvironment and facilitating ECM degradation. Compared with EGCG@MN, CME@MN showed superior efficacy in improving scar morphology and restoring tissue architecture. The combined anti-fibrotic and anti-angiogenic activity of EGCG and the potent PTT properties of $\{Mo_{154}\}$—which simultaneously reduce inflammation and promote collagen degradation—position CME@MN as a promising multitarget therapeutic platform for the management of HS.

Although this temperature range is adequate for achieving an anti-scarring effect, it raises concerns regarding potential injury to adjacent normal skin tissue. To evaluate this possibility, we performed histological examinations of normal skin following a combined MN application and laser irradiation (Fig. S21 in the supplementary information). The analyses showed no evidence of thermal injury—such as necrosis, blistering, or abnormal inflammatory infiltration—within normal skin structures, confirming that the thermal effect remained selective for scar tissue. Furthermore, serum biochemical profiling was conducted to assess the systemic safety of CME@MN. Quantitative analyses of liver function markers—aspartate aminotransferase (AST), alanine aminotransferase (ALT), alkaline phosphatase (ALP), and γ-glutamyl transferase (γ-GT)—as well as kidney function markers creatinine (Cr) and blood urea nitrogen (BUN), showed no statistically significant differences between the treated and control groups (Fig. S22 in the supplementary information). These results confirm the excellent in vivo biocompatibility of the CME@MN system.

3 Conclusions

In this study, we developed a multifunctional, self-assembled nanomedicine CME based on the $\{Mo_{154}\}$ cluster. We incorporated it into a composite MN patch (CME@MN) for transdermal delivery, thereby enabling a multimechanistic therapeutic approach for HSs. The synthesized CME nanoparticles exhibited a uniform spherical morphology with an average diameter of approximately 80 nm, excellent PCE, potent antioxidant capacity, and stability under physiological conditions. The MN array provided consistent mechanical strength, enabling effective penetration of the stratum corneum and facilitating deep delivery of CME with sustained-release characteristics. Cellular studies revealed efficient internalization of CME into scar-related cells, including HUVECs and HKFs, leading to selective inhibition of their viability, while no significant cytotoxicity was observed in THP-1-M0 macrophages. Mechanistic analyses revealed that CME inhibits scar formation through multiple pathways: it scavenges intracellular ROS, acts synergistically with PTT to limit ECM accumulation, promotes collagen remodeling, and induces cell death in HS fibroblasts. In endothelial cells, CME suppressed HUVEC migration and cytokine secretion, reduced inflammatory signaling by downregulating MCP-1, and disrupted the nutrient supply to fibroblasts by inhibiting VEGF and TGF-β1 signaling. Additionally, CME shifted macrophage polarization from the profibrotic M2 phenotype toward the proinflammatory M1 phenotype, consequently inhibiting α-SMA expression in HKFs. In vivo studies revealed targeted accumulation of CME@MN within scar tissue, accompanied by decreased excessive ECM deposition, enhanced collagen organization, and potent inhibition of scar fibroblasts when combined with PTT. The CME@MN system also showed an excellent safety profile, with no significant alterations in body weight or serum biochemical parameters. Although this study elucidates several anti-fibrotic mechanisms, further molecular-level characterization of the underlying signaling pathways remains an important direction for future research. Overall, this study presents an innovative integration of nano-self-assembly technology and MN-based transdermal delivery to achieve a safe, efficient, and multimechanistic therapeutic strategy for HSs, offering significant potential for clinical translation in scar management.

4 Experimental section

Detailed experimental procedures are provided in the supplementary information.

Supplementary Information The online version contains supplementary material available at https://doi.org/10.1631/bdm.2500389.

Acknowledgements The authors acknowledge the financial support from the Fujian Provincial Youth Top-Notch Talent Support Program, China.

Author contributions MYD: investigation and data curation. RFX: writing—original draft and data curation. XBS: investigation. HXL:

investigation. JY: investigation. YLZ: investigation. HJC: resources and supervision. YSL: resources. YG: conceptualization, writing—review and editing, supervision, and funding acquisition. All authors have given approval to the final version of the manuscript.

Declarations

Conflict of interest The authors declare that they have no conflict of interest.

Ethical approval All animal procedures were conducted in compliance with the guidelines of the Animal Care and Use Committee of Fuzhou University (approval number: 2023-SG-033).

Data availability The data that support the findings of this study are available from the corresponding author upon reasonable request.

Use of generative AI tools During the preparation of this work, the authors used DeepSeek in order to improve language readability and check for grammatical errors. After using this tool, the authors reviewed and edited the content as needed and take full responsibility for the content of the publication.

References

1. Peña OA, Martin P (2024) Cellular and molecular mechanisms of skin wound healing. *Nat Rev Mol Cell Biol* 25(8):599–616. https://doi.org/10.1038/s41580-024-00715-1
2. Kohlhauser M, Mayrhofer M, Kamolz LP et al (2024) An update on molecular mechanisms of scarring: a narrative review. *Int J Mol Sci* 25(21):11579. https://doi.org/10.3390/ijms252111579
3. Alster T (2003) Laser scar revision: comparison study of 585-nm pulsed dye laser with and without intralesional corticosteroids. *Dermatol Surg* 29(1):25–29. https://doi.org/10.1046/j.1524-4725.2003.29024.x
4. Li Y, Li M, Qu CJ et al (2022) The polygenic map of keloid fibroblasts reveals fibrosis-associated gene alterations in inflammation and immune responses. *Front Immunol* 12:810290. https://doi.org/10.3389/fimmu.2021.810290
5. De Felice B, Garbi C, Santoriello M et al (2009) Differential apoptosis markers in human keloids and hypertrophic scars fibroblasts. *Mol Cell Biochem* 327(1–2):191–201. https://doi.org/10.1007/s11010-009-0057-x
6. Acosta AC, Joud H, Sun M et al (2023) Keratocyte-derived myofibroblasts: functional differences with their fibroblast precursors. *Invest Ophthalmol Vis Sci* 64(13):9. https://doi.org/10.1167/iovs.64.13.9
7. Mak RKH, Hundhausen C, Nestle FO (2009) Progress in understanding the immunopathogenesis of psoriasis. *Actas Dermosifiliogr* 100:2–13. https://doi.org/10.1016/S0001-7310(09)73372-1
8. Wang XQ, Liu YK, Qing C et al (2009) Hyperactivity of fibroblasts and functional regression of endothelial cells contribute to microvessel occlusion in hypertrophic scarring. *Microvasc Res* 77(2):204–211. https://doi.org/10.1016/j.mvr.2008.08.007
9. Almatroodi SA, Almatroudi A, Khan AA et al (2020) Potential therapeutic targets of epigallocatechin gallate (EGCG), the most abundant catechin in green tea, and its role in the therapy of various types of cancer. *Molecules* 25(14):3146. https://doi.org/10.3390/molecules25143146
10. Riedemann HI, Schmidt MF, Baron JM (2023) Therapy of pathological scars. *J Dtsch Dermatol Ges* 21(7):761–776. https://doi.org/10.1111/ddg.15088
11. Liu JL, Huang MY, Zhang XY et al (2022) Polyoxometalate nanomaterials for enhanced reactive oxygen species theranostics. *Coord Chem Rev* 472:214785. https://doi.org/10.1016/j.ccr.2022.214785
12. Zhou JH, Zhao WC, Miao ZH et al (2020) Folin–ciocalteu assay inspired polyoxometalate nanoclusters as a renal clearable agent for non-inflammatory photothermal cancer therapy. *ACS Nano* 14(2):2126–2136. https://doi.org/10.1021/acsnano.9b08894
13. Jin ZL, Dai WF, Huang ZJ et al (2025) Engineered titanium oxide nanoplatform for targeted photodynamic/photothermal-gas therapy in keloid treatment. *ACS Appl Mater Interfaces* 17(14): 20705–20716. https://doi.org/10.1021/acsami.4c22289
14. Qin J, Guo NN, Yang J et al (2023) Recent advances of metal–polyphenol coordination polymers for biomedical applications. *Biosensors* 13(8):776. https://doi.org/10.3390/bios13080776
15. Duan JW, Chen ZG, Liang XY et al (2020) Construction and application of therapeutic metal-polyphenol capsule for peripheral artery disease. *Biomaterials* 255:120199. https://doi.org/10.1016/j.biomaterials.2020.120199
16. Park G, Yoon BS, Moon JH et al (2008) Green tea polyphenol epigallocatechin-3-gallate suppresses collagen production and proliferation in keloid fibroblasts via inhibition of the STAT3-signaling pathway. *J Invest Dermatol* 128(10):2429–2441. https://doi.org/10.1038/jid.2008.103
17. Wu TP, Li Y, Lee DS (2017) Chitosan-based composite hydrogels for biomedical applications. *Macromol Res* 25(6):480–488. https://doi.org/10.1007/s13233-017-5066-0
18. de Oliveira Pedro R, Ribeiro Pereira A, Oliveira ON et al (2020) Interaction of chitosan derivatives with cell membrane models in a biologically relevant medium. *Colloids Surf B Biointerfaces* 192:111048. https://doi.org/10.1016/j.colsurfb.2020.111048
19. Gao SN, Rao Y, Wang XW et al (2024) Chlorella-loaded antibacterial microneedles for microacupuncture oxygen therapy of diabetic bacterial infected wounds. *Adv Mater* 36(15):2307585. https://doi.org/10.1002/adma.202307585
20. Kim JS, Choi JA, Kim JC et al (2020) Microneedles with dual release pattern for improved immunological efficacy of Hepatitis B vaccine. *Int J Pharm* 591:119928. https://doi.org/10.1016/j.ijpharm.2020.119928
21. Wang XY, Balaji S, Steen EH et al (2020) High–molecular weight hyaluronan attenuates tubulointerstitial scarring in kidney injury. *JCI Insight* 5(12):e136345. https://doi.org/10.1172/jci.insight.136345
22. Guedes G, Wang SQ, Fontana F et al (2021) Dual-crosslinked dynamic hydrogel incorporating $\{Mo_{154}\}$ with pH and NIR responsiveness for chemo-photothermal therapy. *Adv Mater* 33(40): 2170311. https://doi.org/10.1002/adma.202170311
23. Bakun P, Mlynarczyk DT, Koczorowski T et al (2023) Tea-break with epigallocatechin gallate derivatives–powerful polyphenols of great potential for medicine. *Eur J Med Chem* 261:115820. https://doi.org/10.1016/j.ejmech.2023.115820
24. Wang HC, Wang DY, Yu JZ et al (2022) Applications of metal–phenolic networks in nanomedicine: a review. *Biomater Sci* 10(20): 5786–5808. https://doi.org/10.1039/d2bm00969b
25. Müller A, Krickemeyer E, Meyer J et al (1995) $[Mo_{154}(NO)_{14}O_{420}(OH)_{28}(H_2O)_{70}]^{(25\pm5)-}$: a water-soluble big wheel with more than 700 atoms and a relative molecular mass of about 24000. *Angew Chem Int Ed Engl* 34(19):2122–2124.

https://doi.org/10.1002/anie.199521221
26. Wang Y, Kong XP, Li F et al (2022) Mo_{154} synergistically enhanced antibiofilm and antibacterial effects of spermine via coassembly. *ACS Appl Bio Mater* 5(11):5281–5288. https://doi.org/10.1021/acsabm.2c00692
27. Zheng FY, Tan D, Zheng YL et al (2025) A chitosan-based deep tumor-penetrating nano-photothermal agent for enhanced chemo-photothermal combination therapy. *Mater Today Chem* 45:102676. https://doi.org/10.1016/j.mtchem.2025.102676
28. Desai C, Meng XX, Yang DC et al (2011) Effect of solvents on stabilization of micro drug particles. *J Cryst Growth* 314(1): 353–358. https://doi.org/10.1016/j.jcrysgro.2010.11.153
29. Zhong C, Liang GA, Li PT et al (2023) Inflammatory response: the target for treating hyperpigmentation during the repair of a burn wound. *Front Immunol* 14:1009137. https://doi.org/10.3389/fimmu.2023.1009137
30. Li Y, Miao Y, Yang LN et al (2022) Recent advances in the development and antimicrobial applications of metal-phenolic networks. *Adv Sci* 9(27):2202684. https://doi.org/10.1002/advs.202202684
31. Sorkin M, Cholok D, Levi B (2017) Scar management of the burned hand. *Hand Clin* 33(2):305–315. https://doi.org/10.1016/j.hcl.2016.12.009
32. Zhang Q, Shi L, He H et al (2022) Down-regulating scar formation by microneedles directly via a mechanical communication pathway. *ACS Nano* 16(7):10163–10178. https://doi.org/10.1021/acsnano.1c11016
33. Shah S, Alster TS (2010) Laser treatment of dark skin. *Am J Clin Dermatol* 11(6):389–397. https://doi.org/10.2165/11538940-000000000-00000
34. Rabello FB, Souza CD, Júnior JAF (2014) Update on hypertrophic scar treatment. *Clinics* 69(8):565–573. https://doi.org/10.6061/clinics/2014(08)11
35. Li Q, Qin ZL, Chen B et al (2020) Mitochondrial dysfunction and morphological abnormality in keloid fibroblasts. *Adv Wound Care* 9(10):539–552. https://doi.org/10.1089/wound.2019.0988
36. Wang XX, Liu K, Ruan MY et al (2018) Gallic acid inhibits fibroblast growth and migration in keloids through the AKT/ERK signaling pathway. *Acta Biochim Biophys Sin* 50(11):1114–1120. https://doi.org/10.1093/abbs/gmy115
37. Jiang L, Deng Y, Li W et al (2020) Arctigenin suppresses fibroblast activity and extracellular matrix deposition in hypertrophic scarring by reducing inflammation and oxidative stress. *Mol Med Rep* 22(6):4783–4791. https://doi.org/10.3892/mmr.2020.11539
38. Jeschke MG, van Baar ME, Choudhry MA et al (2020) Burn injury. *Nat Rev Dis Primers* 6:11. https://doi.org/10.1038/s41572-020-0145-5
39. Wang XQ, Song F, Liu YK (2017) Hypertrophic scar regression is linked to the occurrence of endothelial dysfunction. *PLoS ONE* 12(5):e0176681. https://doi.org/10.1371/journal.pone.0176681
40. Hou JW, Shi JY, Chen L et al (2018) M2 macrophages promote myofibroblast differentiation of LR-MSCs and are associated with pulmonary fibrogenesis. *Cell Commun Signal* 16(1):89. https://doi.org/10.1186/s12964-018-0300-8
41. Kolliniati O, Ieronymaki E, Vergadi E et al (2022) Metabolic regulation of macrophage activation. *J Innate Immun* 14(1):51–68. https://doi.org/10.1159/000516780
42. Mokos ZB, Jović A, Grgurević L et al (2017) Current therapeutic approach to hypertrophic scars. *Front Med* 4:83. https://doi.org/10.3389/fmed.2017.00083
43. Schachtrup C, Ryu JK, Helmrick MJ et al (2010) Fibrinogen triggers astrocyte scar formation by promoting the availability of active TGF-beta after vascular damage. *J Neurosci* 30(17):5843–5854. https://doi.org/10.1523/JNEUROSCI.0137-10.2010
44. Wilgus TA (2019) Vascular endothelial growth factor and cutaneous scarring. *Adv Wound Care* 8(12):671–678. https://doi.org/10.1089/wound.2018.0796